AAS 14-235

FLOW CONTROL SEGMENT AND LAGRANGIAN COHERENT STRUCTURE APPROACHES FOR APPLICATION IN MULTI–BODY PROBLEMS

Cody R. Short*, Daniel Blazevski†, Kathleen C. Howell‡ and George Haller§

Lagrangian Coherent Structures (LCS) are useful for describing the general flow of a particular system, including specific flow regions advantageous to desirable transport options. The underlying theory that leads to the LCS concept applies to any system that exhibits flow, including the Circular Restricted Three–Body Problem (CR3BP) and other astrodynamical systems. Generally, these models require working within a higher–dimensional phase space. Satisfactory identification of LCS in such systems becomes increasingly challenging, but additional information available from the Cauchy–Green Strain Tensor (CGST) supplies contextual cues to aid in this endeavor or for other applications. Maneuvers seeded from initial Flow Control Segments (FCS), a related concept, can lead to desirable trajectory evolution. These segments provide an option for exploring the phase space and improving maneuver costs that take a spacecraft from an initial location to a target destination. Methods for applying this additional information are explored in this paper.

INTRODUCTION

The concept of Lagrangian Coherent Structures (LCS) has seen application to many dynamical systems in multiple areas of research. These structures represent the most repelling, attracting or shearing material surfaces (i.e., evolving sets of trajectories) that form the hidden skeleton of observed tracer patterns. The majority of LCS analyses have been confined to two–dimensional, planar flows. However, a few rigorous studies have also been completed that establish the theory within three– and n– dimensional flow systems.[1–3] These coherent structures are useful for understanding the overall nature of a system and revealing more suitable trajectory options, a common astrodynamical goal. Examples of LCS employed for astrodynamical analysis and design are supplied by several authors.[4–7] Applications to astrodynamics in the Circular Restricted Three–Body Problem (CR3BP, CRP or restricted problem throughout) require a framework with a minimum of four dimensions (for its planar motion). In the spatial restricted problem or ephemeris gravitational models, analysis requires a six–dimensional state–space, with additional, careful attention to timing considerations in the ephemeris models. With each introduction of additional complexity to the model, satisfactory identification of LCS in these higher–dimensional systems becomes increasingly challenging, but the mathematics used for identifying LCS and related concepts remain useful.

Frequently, LCS are identified using maximal values of the Finite–Time Lyapunov Exponent (FTLE), calculated for trajectories flowing from one region to another. This approach, using FTLE values to identify LCS, is not the only option available for calculating structures in flows. As noted by Peacock and Haller,[8] using FTLE to identify LCS is an often efficient but heuristic approach that should be employed with caution. Some structures revealed by FTLE values represent features that can not be categorized as LCS; or, sometimes

*Ph.D. Student, School of Aeronautics and Astronautics, Purdue University, 701 West Stadium Avenue, West Lafayette, IN 47907-2045.
†Postdoctoral Researcher, Institute for Mechanical Systems, Department of Mechanical and Process Engineering, ETH Zurich, Tannenstrasse 3, Zurich, Switzerland.
‡Hsu Lo Distinguished Professor of Aeronautics and Astronautics, School of Aeronautics and Astronautics, Purdue University, 701 West Stadium Avenue, West Lafayette, IN 47907-2045.
§Professor of Nonlinear Dynamics, Institute for Mechanical Systems, Department of Mechanical and Process Engineering, ETH Zurich, Tannenstrasse 3, Zurich, Switzerland.

FTLE methods may fail to identify features that are, indeed, LCS. Consequently, some FTLE structures may not describe the flow as expected. This ambiguity becomes more severe when additional dimensions are required to model the flow. Therefore, for more clarity, additional information is required to identify features that can be effectively utilized to describe the flow in higher–dimensional systems. Further insight is actually available from the same fundamental mathematics that lead to the FTLE. Specifically, analysis of invariants available from the Cauchy–Green Strain Tensor (CGST), the tensor that supplies FTLE values, can aid in the identification of useful structural information in a given flow.[8,9] Rather than relying solely on the eigenvalues of the Cauchy–Green (CG) tensor in the form of FTLE, exploitation of the eigenvectors is also considered. These eigenvectors are employed in this analysis as Flow Control Segments (FCS) identifying useful directions of motion from an initial point, but they can also aid in the isolation of higher–dimensional LCS.

The problem formulation and implementation of the methodology are described in detail. In the next section, related work is highlighted and the notion of LCS, as well as some underlying mathematical concepts, are discussed. Subsequently, details of particular multi–body formulations and mapping strategies are summarized. Some background material follows directly from Short, Howell and Tricoche[5] as well as Short and Howell.[7] Given an initial point with a known maneuver to transport to a target, exploration of the nearby phase space using flow control segments to shorten segment duration or reduce maneuver costs is considered. Specifically, applied FCS and a targeting strategy as presented by Schroer and Ott[10] and further explored by Grebow,[11] are compared. A more generic example using FCS is also useful. The chief result of this analysis is a system–to–system transfer between two Uranian moons that illustrates the extension of FCS to more complex, nonautonomous systems. Finally, a very brief discussion of CG eigenvectors as related to LCS serves as the last result of the analysis.

LCS FORMULATIONS

Previous contributions

The concept underlying LCS, as well as the name itself, originates with Haller[2,12] and Haller and Yuan.[13] An initial exploration of trajectories in three–dimensional fluid flows with manifolds corresponding to hyperbolic LCS is made by Haller,[2] who also supplies specific criteria to distinguish between structures arising from different effects when identifying LCS.[14] Mathur et al.[15] propose an effective implementation strategy for extracting LCS. In Blazevski and Haller,[1] the problem of detecting arbitrary hyperbolic and elliptic LCS in three dimensions is solved, while Teramoto et al.[3] supply a general, n–dimensional method for computing hyperbolic LCS. Variational techniques for computing LCS are explored in Haller[16] as well as Farazmand and Haller.[17] Incorporating geodesic theory into the framework establishes a criteria for the convergence of LCS, guiding the selection of the appropriate time interval for the numerical simulations to construct LCS.[9]

Given well–established theoretical foundations, the popularity of LCS has quickly expanded and active research continues in multiple disciplines. Simultaneous activities in computer science and visualization are focused on more effective computation and extraction of LCS. Specifically, work by Garth et al.[18] features adaptive mesh refinement for the calculation of FTLE near structures of interest that delivers an improvement in the time efficiency of various approaches for computing LCS. Additional applications of LCS include flow structures in aeronautical weather data, transport in the oceans, computational fluid dynamics, and even human musculoskeletal biomechanics, blood circulation, and airway transport.[19]

The application of FTLE and LCS concepts to astrodynamics has also received some attention. Anderson[20] discusses the application of FTLE over relatively short time spans, denoted by Anderson as the Local Lyapunov Exponent (LLE), to identify sensitive regions along a trajectory. Improved patch point placement for differential corrections using FTLE values is investigated by Harden[21] and Harden et al.[22] Various authors, including Lara et al.,[23] Villac,[24] and Villac and Broschart,[25] all apply fast Lyapunov chaoticity indicators, a metric similar in form to FTLE, for preliminary spacecraft trajectory design and stability analyses in multi–body environments. In an application more closely associated with this investigation, Gawlik et al.[4] examine LCS in the mixed position–velocity phase space of the planar elliptic restricted three–body problem. Additional efforts to apply FTLE and LCS methods in the three–body problem within the context of periapse

mappings are offered by Short, Howell and Tricoche.[5] Pérez et al.[6] also examine the detection of invariant manifolds from LCS in the circular restricted three–body problem. An examination of the impact of increasing the fidelity of the multi–body model on FTLE analysis and LCS guided design is investigated by Short and Howell.[7] Identification of connected orbits in the bicircular and bielliptic four–body problems using LCS is supplied by Oshima and Yanao.[26]

Computing the CGST and FTLE

The Cauchy–Green strain tensor describes the relative stretching of nearby trajectories over a given time interval. As such, the CGST offers a means for identifying relatively larger or smaller directions of expansion. For example, this relative information can be identified from the eigenvalues and eigenvectors of the tensor, that is, the FTLE values that are obtained from the Cauchy–Green eigenvalues. The CGST is computed using the familiar State Transition Matrix (STM), a matrix that describes the impact of initial state variations on the behavior along trajectories over time—essentially a sensitivity matrix or the "Jacobian of the flow map" in other literature. This STM can be calculated by directly observing the effects of perturbed trajectories, or by integrating the first–order variational equations of the system equations of motion.

The flow map, $\phi_{t_0}^{t}(\bar{x})$, represents the state of the system that has evolved to a final time t from an initial state $\bar{x}$ at time t_0. The matrix product, $\frac{d\phi_{t_0}^{t}(\bar{x})}{d\bar{x}_0}^{\mathsf{T}} \frac{d\phi_{t_0}^{t}(\bar{x})}{d\bar{x}_0}$, is the Cauchy–Green strain tensor,[27] and the individual matrix, $\frac{d\phi_{t_0}^{t}(\bar{x})}{d\bar{x}_0}$, is the STM evaluated along the arc at time t (here, $^{\mathsf{T}}$ indicates the matrix transpose). Since the state transition matrix supplies the evolution of infinitesimal perturbations to an initial state of the system, the Cauchy–Green strain tensor represents a natural object to study that reveals the growth or decay of these perturbations. For example, if several adjacent, initial state vectors are separated by small perturbations and subsequently evolved for a prescribed time, the Jacobian is estimated (here, using only two dimensions for illustration) as described by Haller[2] via finite differencing such as,

$$\left.\frac{d\phi_{t_0}^{t}(\bar{x})}{d\bar{x}_0}\right|_{(i,j)} = \begin{bmatrix} \frac{x_{i+1,j}(t)-x_{i-1,j}(t)}{x_{i+1,j}(t_0)-x_{i-1,j}(t_0)} & \frac{x_{i,j+1}(t)-x_{i,j-1}(t)}{y_{i,j+1}(t_0)-y_{i,j-1}(t_0)} \\ \frac{y_{i+1,j}(t)-y_{i-1,j}(t)}{x_{i+1,j}(t_0)-x_{i-1,j}(t_0)} & \frac{y_{i,j+1}(t)-y_{i,j-1}(t)}{y_{i,j+1}(t_0)-y_{i,j-1}(t_0)} \end{bmatrix}, \tag{1}$$

where the indices i and j indicate relative initial perturbations in x and y, respectively.

Various schemes exist for calculating the Jacobian, including numerical integration of the variational equations, direct calculation from a grid of points (as in Equation (1)) or through the use of an auxiliary grid as described by Farazmand and Haller.[17] Direct computation from a grid of points that covers the domain of the simulation allows for the determination of the FTLE in systems where variational equations are not available. Selecting an appropriate grid spacing facilitates the identification of LCS consistent with the order of the grid spacing. A mesh with inadequate resolution may exclude some structures. However, an auxiliary grid that brackets each of the primary grid points increases the accuracy of the resulting Jacobian.

Available from the CGST, the finite–time Lyapunov exponent*, is generally the most common metric for identifying LCS. Relatively high values of the FTLE may, in some cases, indicate LCS. The FTLE essentially measures the stretching between adjacent trajectories over a prescribed time interval. Mathematically, the calculation of the FTLE is fairly straightforward—it is the largest normalized eigenvalue of $\sqrt{\frac{d\phi_{t_0}^{t}(\bar{x})}{d\bar{x}_0}^{\mathsf{T}} \frac{d\phi_{t_0}^{t}(\bar{x})}{d\bar{x}_0}}$, i.e., the matrix spectral norm of the Jacobian with respect to the initial variations. Thus, the expression for the FTLE is,

$$\lambda = \frac{1}{|T|} \ln \tilde{\lambda}_{\max} \left(\sqrt{\frac{d\phi_{t_0}^{t}(\bar{x})}{d\bar{x}_0}^{\mathsf{T}} \frac{d\phi_{t_0}^{t}(\bar{x})}{d\bar{x}_0}} \right), \tag{2}$$

where $\tilde{\lambda}_{\max}()$ is the operation that extracts the largest eigenvalue of the operand. The parameter $T = t - t_0$ represents both the truncation time for the FTLE and a means of normalizing the FTLE value.

*Here *the FTLE* refers to the largest finite–time Lyapunov exponent, which is generally of principle interest in FTLE/LCS analysis. However, some consideration is also given to the smallest FTLE in the literature.[28]

Flow control segments

The eigenvectors of the Cauchy–Green tensor also yield further information. For example, examination of the eigenvector structure of the CGST within the context of coherent structures implies the relationship that $\boldsymbol{\xi}_n \widehat{=} \lambda_n$ is everywhere orthogonal to repelling LCS in planar cases,[9,16] where $\boldsymbol{\xi}_n$ is the eigenvector associated with the largest eigenvalue, λ_n; thus, in this case $n = 2$ or $n = 4$. Blazevski and Haller demonstrate the extension of this concept, with additional constraints, to three–dimensional flows.[1] More generally, $\boldsymbol{\xi}_n$ reveals the direction of greatest expansion along a particular trajectory arc. Therefore, the associated eigendirection is the optimal direction for seeding flow control segments.

The notion of control segments is introduced by Shinbrot et al.[29] with further extensions by Schroer and Ott.[10] In Schroer and Ott, the authors employ small arc segments or circles taken about specific points on a Poincaré map to join two periodic orbits from different regions in the chaotic CRP phase space. Working in the planar CRP, a map is defined in terms of position and velocity Cartesian x components in the rotating frame. A strategy where a segment and circle are simultaneously iterated forward from the vicinity of an initial orbit and backward from a target orbit region on the map is utilized. As the segments are advected under the flow, their pre– or post–images grow until, after some (likely different) number of forward and backward iterations, an intersection occurs. This process is illustrated in Figure 1, reproduced from Schroer and Ott[10] with permission. Such an intersection is a connection in all components of the planar CRP state

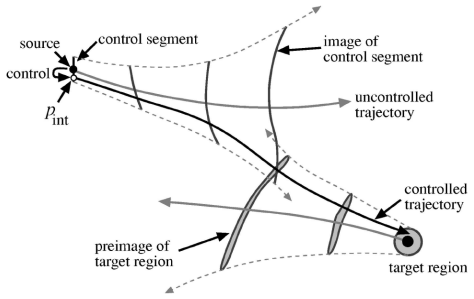

Figure 1. Forward–Backward Method of Shinbrot et al.[29] (Figure Reproduced from Schroer and Ott[10] with Publisher's Permission)

and represents an end–to–end trajectory joining the orbits with small velocity discontinuities at departure and insertion. In Grebow,[11] the example from Schroer and Ott is revisited. Grebow observes that the natural stretching of the target circle quickly collapses it to an arc. Thus, the process may be equally well served by employing arc segments for both forward and backward evolution.

In the present paper, similar flow control segments are constructed along the eigenvector, $\boldsymbol{\xi}_n$, associated with the largest eigenvalue of the Cauchy–Green tensor. Assuming an appropriate time scale for calculating the CGST, stretching occurs in the phase space along the eigenvector, $\boldsymbol{\xi}_i$, proportional to $\sqrt{\lambda_i}$, thus $\boldsymbol{\xi}_n$ supplies the most–stretching direction in the flow, and represents the optimal choice for divergent behavior. Consequently, the images resulting from evolving $\boldsymbol{\xi}_n$–aligned segments should intersect after fewer iterations yielding a shorter time–duration transfer.

Lagrangian coherent structures

Lagrangian coherent structures are defined as influential material surfaces (sets of trajectories) that locally induce the largest deformation of nearby phase–space elements.[16] They exist in the form of hyperbolic and shear LCS where they display the largest attraction, repulsion or shear in a neighborhood. This notion of structures that characterize the flow in a region represents a powerful insight for describing useful options for trajectory design. The insight is particularly applicable in astrodynamical problems since LCS exist in complex settings where other, more restricted, options are not available. For example, the stable and unstable

manifold tubes associated with unstable periodic orbits in the CRP that are frequently exploited to guide trajectory design are not available in higher–fidelity ephemeris models. In fact, in autonomous systems, there exists a correlation between LCS and invariant manifolds. However, classic stable and unstable manifolds are only guaranteed to act as centerpieces of phase–space deformation over infinitely long times. Over finite times, LCS play this role, evolving with the flow even in autonomous systems. As the finite–time interval of their extraction grows, LCS gradually converge to classic invariant manifolds, should the latter exist in the flow. Even in the restricted problem, options that employ manifold structures to guide the flow from some generic point may not be readily available. However, given any initial state in a system, a CG tensor can be evaluated and information can be deduced regarding the behavior of the flow resulting from the evolution of such a state. Structural information may be obtained in a general sense and LCS identified if they exist. A brief discussion of some common options for constructing Lagrangian coherent structures follows.

Ridges in FTLE scalar fields. In practice, an entire field of FTLE values is often computed and displayed on a map or section. Then, comparisons of FTLE values across a relatively large area are possible. Specifically, regions characteristic of similar FTLE values are identified. A single individual region may appear markedly different, in terms of FTLE value, than other regions within the field. Bounding these regions are height ridges corresponding to relatively large FTLE values. Such ridges are defined as curves where the FTLE values are maximal with respect to the largest principle curvature. These ridge values are largest with respect to the sides of the ridge but not necessarily along the top of the ridge where they may be greater or less than neighboring ridge values. Height ridges, their significance and computation, are given greater treatment by Eberly et al.[30] These strongest FTLE ridges can represent Lagrangian coherent structures, and act as boundaries in the flow separating regions of fundamentally different qualitative behavior.

Streamlines/surfaces of CG vector fields. While the FTLE is a convenient and relatively well–behaved measure of the stretching between neighboring trajectories, it represents only part of the information available from the Cauchy–Green tensor. Other valuable insights are accessible directly from the eigenvalues and eigenvectors of the tensor. In two–dimensional flows, Haller and Beron–Vera[9] establish various vector fields with the associated streamlines that correspond to transport barriers or LCS. Haller and Beron–Vera elaborate on exploiting all of the eigenvalues, eigenvectors and composite eigenvalue–eigenvector fields to identify different types of structures. For example, the particular streamlines that correlate with hyperbolic LCS are available from the eigenvector field consistent with the smallest eigenvalue. The vector field associated with this smallest eigenvalue is a strain field and yields a particular type of streamline, i.e., those denoted as strainlines. The strainlines with the smallest point–wise geodesic deviation are identified as hyperbolic transport barriers. Moreover, a selected tolerance on the value of the geodesic deviation supplies a criterion to identify convergence of the LCS and to calibrate algorithms for detecting such structures. In higher–dimensional systems, the streamline concept extends to streamsurfaces and, similar to the planar case, LCS are constructed by isolating the streamsurfaces that align with or are normal to certain eigenvectors of the Cauchy–Green tensor.[1]

SYSTEM MODELS

The computation of the CGST is not contingent on any assumptions in the derivation of the system differential equations and, thus, can be applied to systems modeled with various levels of fidelity. Analysis based on the Cauchy–Green tensor remains valid regardless of the complexity of the model. Here, FCS are investigated in examples within the context of the circular restricted problem as well as a bicircular four–body system. Selected results are transitioned through various levels of fidelity and are ultimately validated in a partial ephemeris model. Some necessary considerations for each model are summarized.

The restricted three–body model

Some key space environments involve multiple gravity fields, thus, it is often necessary to incorporate as many of these gravity fields as possible into the governing models to ensure accurate simulation and to capture the essential features of the dynamical interactions. Models involving more than two gravitating point–mass bodies, however, offer no analytical solutions, and introduce additional complexities, which may be small but significant. Formulating the problem in terms of three bodies produces a model sufficiently complex to reveal many important characteristics while remaining tractable. However, the general three–body problem

possesses no closed–form solution.[31] Thus, additional simplifications, such as those consistent with the CRP, offer significant insight. The CRP incorporates only the effects of the masses of the two larger primaries (for example, the Earth and the Moon as they evolve on mutual circular orbits) on a third, much smaller mass, such as a spacecraft.

A mathematical definition for the CRP is required for numerical simulation. The two primary bodies that appear in the model are designated as P_1 and P_2. Position variables, x, y, and z describe the position of the third body, the spacecraft, with respect to the barycenter of the primary system, which also serves as the origin of the rotating and inertial reference frames. The system mass parameter is represented by $\mu = \frac{m_2}{m_1+m_2}$, a function of the masses of the primary bodies. Additionally, distances between the third body and the two primaries are denoted r_{i3}. Specifically, in a coordinate frame that rotates coincident with the circular motion of the primaries, a system of differential equations that describes the motion of the third body incorporates the potential function,

$$U^* = \frac{1-\mu}{r_{13}} + \frac{\mu}{r_{23}} + \frac{1}{2}(x^2+y^2), \tag{3}$$

and is written,

$$\ddot{x} = \frac{\partial U^*}{\partial x} + 2\dot{y}, \quad \ddot{y} = \frac{\partial U^*}{\partial y} - 2\dot{x}, \quad \ddot{z} = \frac{\partial U^*}{\partial z}, \tag{4}$$

where the first derivatives in x and y appear as a result of Coriolis acceleration.

The equations of motion in the restricted problem are consistent with Szebehely[32] where they admit a single integral of the motion. This integral is termed the Jacobi integral and is represented as C in this analysis,

$$C = 2U^* - v^2, \tag{5}$$

where $v^2 = \dot{x}^2 + \dot{y}^2 + \dot{z}^2$, that is, the square of the magnitude of the relative velocity. This integral allows for a reduction of order in the problem, and frequently serves in an important role in the definition of maps. The Jacobi integral reveals boundaries on the motion of the third body in the restricted problem. These boundaries are defined when the velocity in Equation (5) is zero, separating regions of real and imaginary velocities. An example of the Jacobi limiting boundaries, or Zero Velocity Curves (ZVC) in the x–y plane (plotted in black), is depicted in Figure 2 along with the two libration points near the second primary (in this case, Saturn at $50\times$ scale in the Sun–Saturn system). These types of boundaries on the motion are intimately associated with the definitions of the maps employed here.

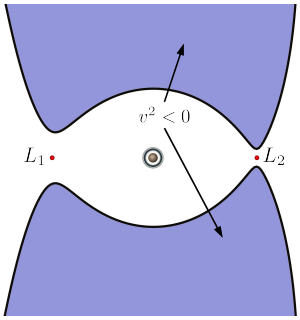

Figure 2. Zero Velocity Curves in the P_2 Region

The restricted problem represents a model of sufficient complexity to exhibit regions of both chaotic and ordered behavior. Generally, the focus of analysis in this model is understanding and exploiting any dynamical structures that are associated with the chaotic regions to identify useful trajectory arcs. The CRP model is frequently suitable to yield first–order mission design solutions, but useful information is often difficult to isolate amidst the chaos.

The bicircular four–body model

A simplified four–body model, similar to the model utilized by Koon et al.[33] and further explored by Blazevski and Ocampo,[34] is also employed here. This model incorporates the influence of a third massive body simultaneously with the dynamical effects of the two primary bodies in the circular restricted problem. For a particular planet–moon example, Uranus, Titania, Oberon and a spacecraft comprise the four–body system. A specific orientation of the relative geometry of such a system, e.g., in a Uranus–Titania rotating frame, appears in Figure 3. The orbital angle that defines the initial position of the fourth body, measured counter–clockwise with respect to the rotating x axis, is denoted θ_0 (in the example figure, $\theta_0 = \frac{\pi}{4}$ radians, or 45^o). Under this model, all three massive primaries describe circular orbits about the barycenter of the

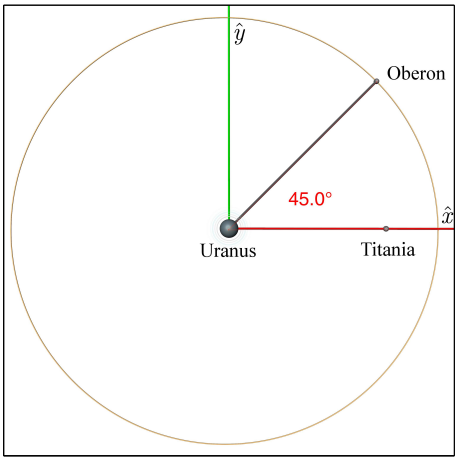

Figure 3. The Bicircular Four–body Problem

first and second primaries (Uranus, Titania). The additional massive primary is designated P_4 (Oberon). Although the system is not coherent, the Newtonian inverse–square gravity of P_4 acts on the spacecraft in addition to the gravitational effects of the two CRP primaries. The third primary body does not affect the circular Keplerian orbits of the other primaries. The equations of motion remain the same as Equations (4), but the potential function is now,[35]

$$U^* = \frac{1-\mu}{r_{13}} + \frac{\mu}{r_{23}} + \frac{\mu_4}{r_{43}} + \frac{1}{2}(x^2 + y^2), \tag{6}$$

where $\mu_4 = \frac{m_4}{m_1+m_2}$.

Such a four–body model, while still incorporating significant simplifications, introduces an important transition. The presence of the perturbing fourth body results in a nonautonomous system. This change in the nature of the system decreases the applicability of many of the dynamical systems tools that are available in the CRP, while completely removing others. A constant of the motion, and, consequently, a convenient expression for bounds on the motion, is no longer available. Due to the time–dependent nature of the underlying flow, careful consideration is now focused on the initial system geometry.

Partial ephemeris model

A partial ephemeris model is selected to be generally consistent with the previous models. This higher–fidelity model, similar to the model employed by Pavlak and Howell,[36] is constructed to validate the solution obtained from simpler models by incorporating position histories for the primary bodies supplied by the JPL DE405 ephemerides. The model is designated a “partial” ephemeris model because only the primary bodies

of interest, and no higher–order perturbing effects, are included. The governing equations are then derived as the n–body relative equations of motion,

$$\ddot{\overline{r}}_{qs} = -\frac{\mu_{2b,s} + \mu_{2b,s}}{r_{qs}^3}\overline{r}_{qs} + \sum_{\substack{j=1 \\ j\neq s,q}}^{n} \mu_{2b,j}\left(\frac{\overline{r}_{sj}}{r_{sj}^3} - \frac{\overline{r}_{qj}}{r_{qj}^3}\right). \tag{7}$$

Here, μ_{2b} is the familiar mass parameter from the two–body problem, nondimensionalized as appropriate. The position vector, $\overline{r}_{qj}$, indicates the position of the j^{th} body with respect to the central body, q; the subscript s is associated with the spacecraft. In this model, states defined in the restricted problem are transitioned to body–centered J2000 states via an instantaneous rotating frame defined by ephemerides.

This partial ephemeris model naturally involves six–dimensional state vectors and trajectory propagation proceeds in all spatial dimensions. Additionally, computation of the CGST employs auxiliary "grid" points about each state variable. Thus, in this model, one CGST computation involves the propagation of 12 perturbations. Notwithstanding these spatial considerations, since the maps are transitioned from the planar lower–fidelity model, their domain remains the same.

These models illustrate the wide applicability of LCS analysis to different types of systems. Ultimately, this extensibility indicates that this type of strategy can be employed for a full–ephemeris design and analysis. Such capability is supported by previous literature in other fields which describes the Cauchy–Green tensor as a tool for directly analyzing empirical flow results (when no underlying dynamical model is available).[15,19]

MAPS

Mapping analysis within the context of multi–body regimes has proven to effectively reveal design options that are otherwise difficult to identify (see, for example, Davis and Howell[37]). Some advantages of a map–based approach include a broader view of the design space as well as a "cleaner" visual that offers easier categorization of the behavior in a specific region. The maps employed in this analysis generally employ relatively well–known mapping strategies. These maps offer a Lagrangian perspective and essentially reflect the fate of a grid of initial conditions in terms of their FTLE values associated with some propagation time.

State–space maps

Analysis in many systems involves a traditional Poincaré mapping to create a puncture plot that facilitates the investigation. Such a map reveals salient information by reducing the dimension of the system and alleviating obscuration. Under this Poincaré mapping approach, a hyperplane corresponding to some value of a single state variable is defined. A grid supplies the relationship between two other state variables, and the fourth state is constrained by a system integral.

While there are many possible map representations available for observing the behavior in a system, strategies frequently involve the investigation of position–velocity phase spaces. For example, a map can be plotted in terms of a position variable and its associated velocity component. Maps in the y–$\dot{y}$ and x–$\dot{x}$ phase spaces are both used in this investigation, the former employed for FTLE maps and latter for puncture plots.

Stroboscopic maps

Traditional stroboscopic maps are constructed as Poincaré maps with a hyperplane condition selected as a particular time, for example, the characteristic period of a system. Alternatively, this time condition may be arbitrarily defined. Crossings in this type of map are recorded every T time units, where T is the time condition defined for the hyperplane. Such a stroboscopic map may be more insightful with repeating behavior. A common application of FTLE maps that is consistent with the definition of Lagrangian coherent structures is, effectively, a single iteration of a stroboscopic map. That is, LCS are defined as structures emerging when the flow map is evaluated at the same final time, T, for all initial states. This type of map highlights the stretching of nearby trajectories at a specified time downstream and allows for more direct comparison across an entire field of FTLE values.

One essential value of the finite–time Lyapunov exponent for predicting behavior is captured by examining large groupings of FTLE values in a region. This approach leads directly to creating maps of FTLE values.

Aspects from the various types of mapping strategies can be combined to effectively illustrate the flow in an astrodynamical model. The information that emerges from these maps is then incorporated into different phases of mission design and analysis.

APPLICATIONS

The insight revealed from the Cauchy–Green tensor is well–suited to identify trajectories that exhibit certain desirable characteristics. A few examples are produced to demonstrate the potential strategies for utilizing this insight. Specifically, targeting, or control, segments are developed both with and without the flow context provided from the CGST. This comparison is followed by a generalized example of the implementation of flow control segments. The main result of the paper highlights the extensions of these schemes to nonautonomous systems. Finally, the potential application of flow–based contextual cues to systems of higher dimensionality is noted.

FCS targeting

The forward and backward time–advection of small segments bracketing a control point, denoted control segments, is investigated by Shinbrot et al.,[29] further expanded by Schroer and Ott[10] and revisited by Grebow.[11] These control segments are created as small segments in a particular velocity component without consideration of the underlying flow behavior. This initialization approach is a consequence of the desire to vary velocity only in a "feasible" direction while restricting any variation in initial or final position to zero. However, small adjustments in the direction of the phase space that naturally leads toward greater flow divergence augments the approach of joining forward and backward trajectory segments, producing a trajectory that can be subsequently corrected with a differential corrections scheme. Thus, control segments constructed exploiting the flow context may yield a better result depending on the desired trajectory characteristics.

A comparison of control segment applications with and without flow–based context. Schroer and Ott produce an example of forward–time control segment advection and backward–time target region advection to join two periodic orbits in the Earth–Moon circular restricted three–body problem. In the following example, the mass–parameter and energy levels are consistent with Schroer and Ott ($\mu = 0.0123$, and $C = 3.17948$). The initial and final periodic orbits are generated numerically after observation of the trajectory characteristics as elaborated by Grebow. The following orbits and the associated map representations compare closely with Grebow. The initial orbit, in this case, is a period–3 orbit and is depicted in green in Figure 4(a), along with the final orbit about the Moon (red). The initial points on both orbits are marked with small gold spheres

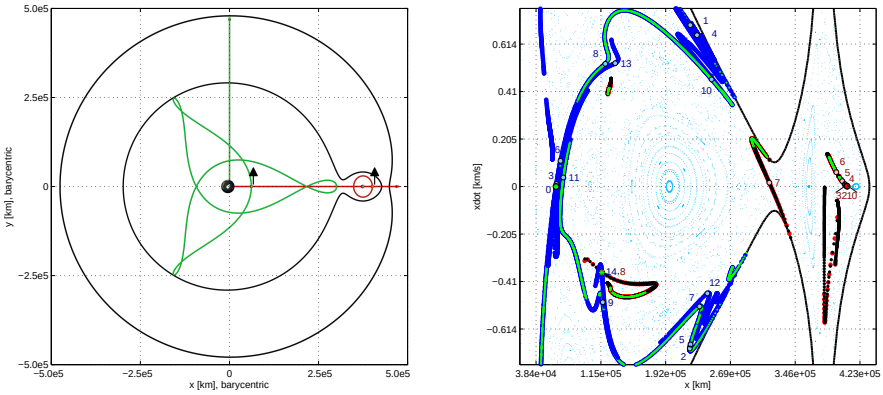

(a) Candidate Orbits for Connection

(b) Orbits on the x–$\dot{x}$ Poincaré Section $y = 0$

Figure 4. Orbits and Control Segments

and black arrows on the x axis; the forward time evolution from both points is in the positive y direction.

Moreover, the trajectories are subsequently represented as fixed points (numbered "0" and marked with green and red asterisks) on the x–$\dot{x}$ phase–space Poincaré map in Figure 4(b). From the control points on the map, small segments (magnitude 1×10^{-4}) are created along the map–space components of the eigenvector associated with the largest eigenvalue of the Cauchy–Green tensor, that is, along $\boldsymbol{\xi}_2$, in this case. Here, the CGST is computed only with respect to the map via finite–difference derivatives in x and $\dot{x}$. The control segments are evolved under the flow of the system backward and forward in time from the lunar–proximal control point and triply–periodic control point, respectively. For comparison with the previous investigations of this specific example, segments along only $\dot{x}$ as well as a segment defined as a circle about the control point near the Moon are also integrated. The images of each of these curve evolutions corresponding to iterations of the map also appear in Figure 4(b). The curves are colored based on their initial nature: green curves result from advection of purely $\dot{x}$ segments, red and blue curves from the $\boldsymbol{\xi}_2$ aligned segments, and, in the case of the circular target region, black points mark the associated curves. Observation of the initial backward iterations of the circular target region reveals that it quickly deforms to align with the $\boldsymbol{\xi}_2$ segment. Later iterations in both time directions reflect longer curves associated with the flow aligned control segments; the green points resulting from the initial $\dot{x}$ segments require more iterations before an intersection is observed. Also marked on Figure 4(b) are the map crossings associated with trajectory arcs that intersect after 14 forward iterations from a perturbation off the triply–periodic orbit and 8 backward iterations from the lunar orbit step–off.

The trajectory arcs necessarily include discontinuities at the departure and arrival points. Since perturbations are introduced along the eigendirection, these discontinuities are in position as well as velocity. Moreover, rather than employ an iterative scheme such as bisection to refine the intersection between the forward and backward arcs, a slight discontinuity is allowed at this point as well. These discontinuities are resolved by implementing a parallel shooting differential corrections scheme as described by Pavlak.[38] Upon convergence of the corrections process, the only remaining discontinuities are the requisite velocity changes to satisfy the transfer. Figure 5 includes views of the backward arc and the differentially corrected CRP solution. The

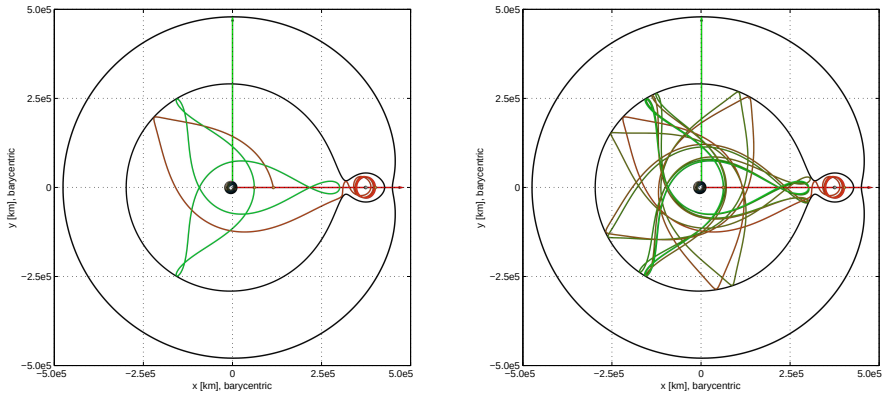

(a) Backward Trajectory Arc (b) Corrected CRP Solution

Figure 5. Connected Forward and Backward Segments

connection point is visible as a third gold sphere also marked with a black arrow on the x axis ($x \approx 100{,}000$ km). The trajectory evolution in time is reflected in color by a gradual transition from green to red. The maneuver requirement at departure is 1.99 $\frac{\text{m}}{\text{s}}$, while the Δv upon arrival is 1.04 $\frac{\text{m}}{\text{s}}$ (total: 3.03 $\frac{\text{m}}{\text{s}}$). These maneuver costs compare with one of the examples from Schroer and Ott at 0.62 $\frac{\text{m}}{\text{s}}$ and 2.61 $\frac{\text{m}}{\text{s}}$, respectively, for a total of 3.23 $\frac{\text{m}}{\text{s}}$. They likewise compare with figures reported by Grebow for a somewhat qualitatively different solution—0.39 $\frac{\text{m}}{\text{s}}$ and 1.46 $\frac{\text{m}}{\text{s}}$ (total: 1.85 $\frac{\text{m}}{\text{s}}$). A significant difference, and potential advantage of the FCS approach, is a shorter time–of–flight. Each example reported by previous sources requires more than 290 days; the sample transfer here is completed in 265 days. This shorter duration is a direct consequence of the method reaching an intersection in fewer iterations given maximal stretching from $\boldsymbol{\xi}_2$–aligned segments.

A validation of the given solution concludes this example. For a carefully selected initial epoch, the CRP solution is transitioned into the higher–fidelity ephemeris n–body model. In this case, only the ephemerides of the Earth and Moon are included. Views of the transitioned solution appear in Figure 6; the states are numerically corrected for velocity and position continuity to within $3{\times}10^{-6}$ $\frac{\text{m}}{\text{s}}$ and 0.8 m. The ephemeris

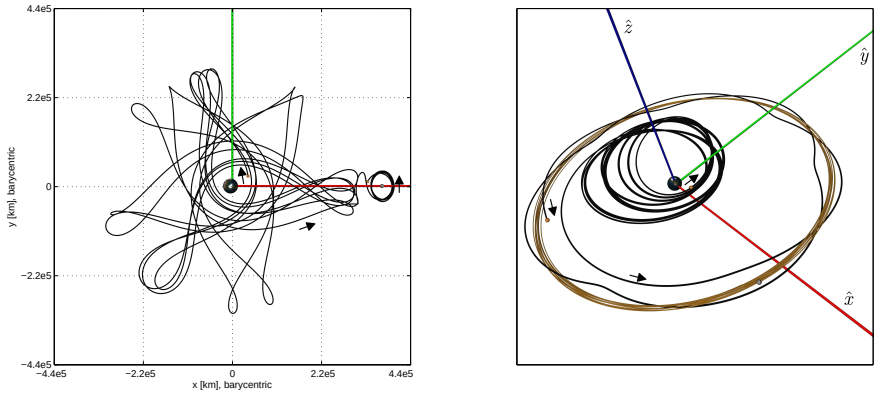

(a) Rotating View (b) Inertial View

Figure 6. Corrected Ephemeris Solution

solution necessarily experiences fully three–dimensional motion with maximum out–of–plane excursions greater than 2000 km. The convergence of the solution in the higher–fidelity model lends support to the process of seeking solutions by perturbing in position space as well as velocity space. Not only can the relatively complex solution be corrected in the simplified three–body model, but it can be replicated in a system that mimics the actual three–dimensional behavior of the primary bodies.

A more general case. Before leaving the three–body problem as the primary model for analysis, another example serves to further reinforce the extensibility and flexibility of the flow control segment approach for identifying transfer trajectories. In this case, still in the Earth–Moon CRP, the system energy level is increased as reflected by a smaller Jacobi constant value of $C = 3.05$. Given this energy level, both the gateway allowing passage into the lunar region as well as the gateway offering exit from the system are open. That is, trajectories can transit through both the L_1 and L_2 regions. Consequently, the chaoticity of the resulting map space is increased.

To illustrate the continued applicability of the control segment approach, two map points are selected arbitrarily as control points for this example. These points are marked as "0" in Figure 7. In this case, there are no initial or terminal orbits, but rather the situation reflects the general notion of a spacecraft currently at some arbitrary state while it is desirable for it to be elsewhere in the state–space. Subsequent iterations from the initial states of the associated $\boldsymbol{\xi}_2$ (1×10^{-4}) segments are also numbered in Figure 7. After 10 forward iterations (blue) and 7 backward iterations (red) a near intersection is observed. The discontinuity at the intersection point is significant, however, the end–to–end trajectory is otherwise well–behaved and the differential corrector converges upon a solution quickly. As before, this trajectory is transitioned to the higher–fidelity model. In this example, since there are no revolutions about the Moon, the ephemeris solution more closely resembles the CRP solution. The corrected CRP and ephemeris trajectories appear (both in the rotating frame) in Figure 8. In the solution computed in the restricted problem, a maneuver of magnitude 0.70 $\frac{\text{m}}{\text{s}}$ is required at the departure point, while a 0.76 $\frac{\text{m}}{\text{s}}$ maneuver is required upon arrival at the final state (total: 1.46 $\frac{\text{m}}{\text{s}}$ with a time–of–flight just under 372 days). This example further establishes the FCS targeting approach and demonstrates its application in more generic situations.

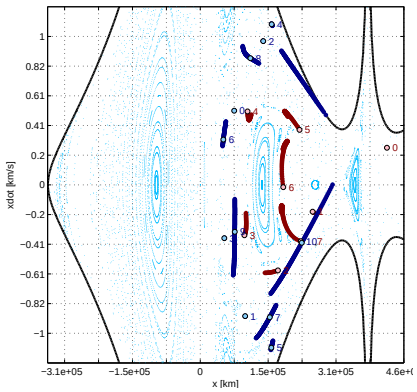

Figure 7. Generic Control Points and Advected Curves

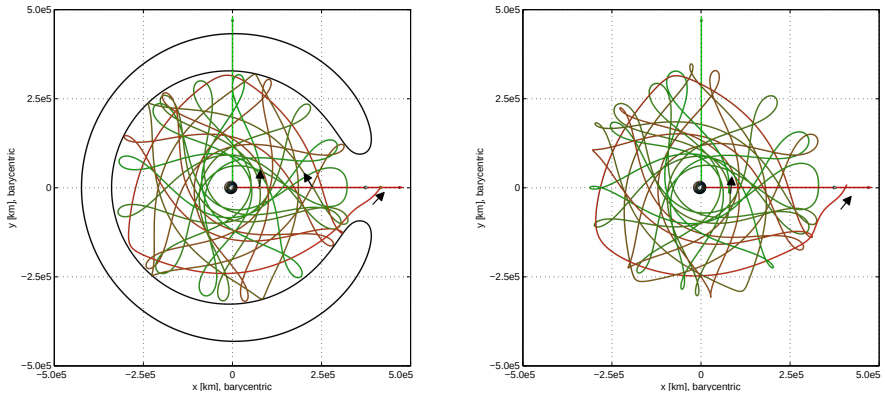

(a) Corrected CRP Solution (b) Corrected Ephemeris Solution

Figure 8. Connection of Arbitrarily Selected Map Points

System–to–system FCS example

The major result of this paper is illustrated by an example involving the flow control segment approach for targeting trajectories in the bicircular four–body problem. This model is selected because it provides a convenient context for a system–to–system transfer and for its increased complexity as a nonautonomous system. Specifically, the Uranus–Titania–Oberon system is selected for its mass and distance characteristics. Titania and Oberon are the same order of magnitude in mass, possessing two–body gravitational parameters of Gm =228.2 km^3/s^2 and Gm =192.4 km^3/s^2, respectively (Uranus: 5,793,939 km^3/s^2).[39] Moreover their orbits are relatively close to Uranus and each other with semi–major axes of $\sim 4.36 \times 10^5$ and $\sim 5.83 \times 10^5$ kilometers with respect to Uranus. Together, these considerations supply significant perturbing influences from the third primary, i.e., Oberon, to the behavior from the perspective of the Uranus–Titania system (as well as significant perturbations from Titania on motion as observed in the Uranus–Oberon system). Koon et al.[33] introduce a similar system–to–system analysis using manifolds in the patched circular restricted problems of Jupiter–Europa and Jupiter–Ganymede.

For an illustration of the concept, both Uranian satellites are depicted in Figure 9 in the Uranus–Titania rotating frame, along with artificial (in this model and frame) zero–velocity curves for energy levels that supply the necessary gateway dynamics in the CRP. Oberon's circular orbital path also appears in gold.

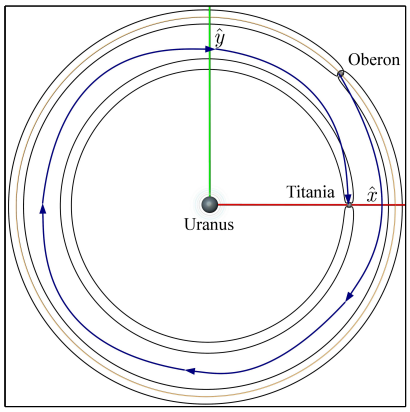

Figure 9. System–to–System Transfer Illustration (Uranus–Titania Rotating Frame)

The objective is a trajectory that experiences a revolution about Oberon and departs toward Titania, ultimately concluding with a revolution of Titania after following a transfer similar to the blue "path" in Figure 9. Despite the depiction in Figure 9, there are actually no convenient bounds on energy like those available in the restricted problem. Taken in turn, both Titania and Oberon are treated as the "additional" body, thus, the third massive primary may circumscribe (or be circumscribed by) the other. In Figure 9, Oberon is placed at an initial angle of $\frac{\pi}{4}$ radians with respect to x axis of the rotating Uranus–Titania frame (or, viewed alternately, Titania is depicted at $-\frac{\pi}{4}$ radians in the Uranus–Oberon rotating frame). For the sake of consistency, trajectory segments departing the Oberon region and moving inward toward Titania and Uranus are phased such that Oberon initiates in the geometry described by Figure 9. Trajectories that depart the Titania region outward toward Oberon (i.e., in reverse time) reflect the effects of Oberon originating elsewhere than at $\frac{\pi}{4}$ radians, barring coincidence.

To isolate the desired behavior near Oberon and Titania, surfaces of section (generically, Σ) are constructed in the y–$\dot{y}$ phase space just beyond the gateways near L_1 and L_2, as illustrated in Figure 10. The sections are defined consistent with $-0.035 \leq y \leq 0.035$ nondimensionalized units (nd) and $-0.03 \leq \dot{y} \leq 0.03$ nd.

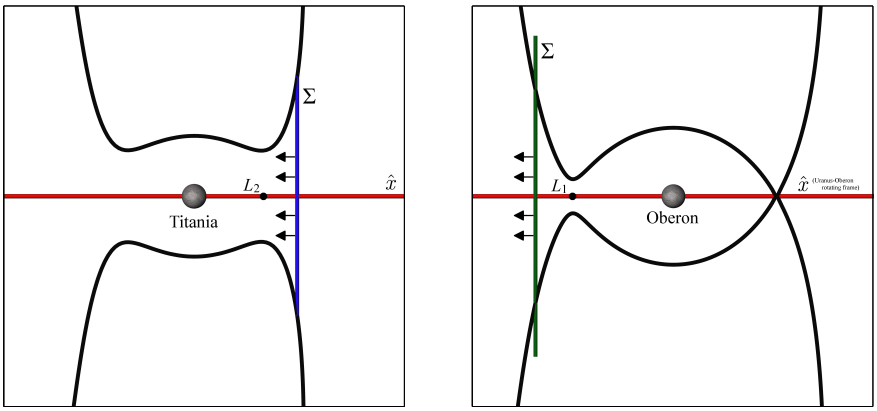

(a) $\Sigma : x = 1.03$ nd; Uranus–Titania Rotating Frame (b) $\Sigma : x = 0.97$ nd; Uranus–Oberon Rotating Frame

Figure 10. Surfaces of Section for FTLE Grids

These ranges translate to $-15500 \lesssim y \lesssim 15500$ km and $-0.1094 \lesssim \dot{y} \lesssim 0.1094$ $\frac{\text{km}}{\text{s}}$ with $\Sigma : x \approx 449000$ km (1.03 nd) in the Uranus–Titania system. In the Uranus–Oberon system the section definition dimensionalizes to $-20500 \lesssim y \lesssim 20500$ km and $-0.0945 \lesssim \dot{y} \lesssim 0.0945$ $\frac{\text{km}}{\text{s}}$ with $\Sigma : x \approx 566000$ km (0.97 nd). In both cases, $\dot{x}$ is recovered from the CRP Jacobi constant consistent with the ZVC depicted in Figures 9 & 10 (in fact, each value of C equals 3.004316 in its respective system). Specifically, the negative root is selected in the evaluation of $\dot{x}$ for both maps. That is, $\dot{x}$ is directed (for forward time evolution) "inward" toward Uranus as indicated by black arrows in Figure 10. As demonstrated by Short and Howell,[7] the associated initial conditions (IC) can be transitioned and evolved in another model—in this case, the IC are advected in the four–body model. Values of FTLE, resulting from forward integration for 10 nondimensional time steps (∼13.8 days) into the Titania region as well as backward evolution toward Oberon (10 nd; ∼21.4 days), appear colored consistent with the color scales in Figure 11(a–b). The two states investigated in this example are marked with black dots in Figure 11(a–b). A computational aside is illustrated by Figure 11(c–d).* An

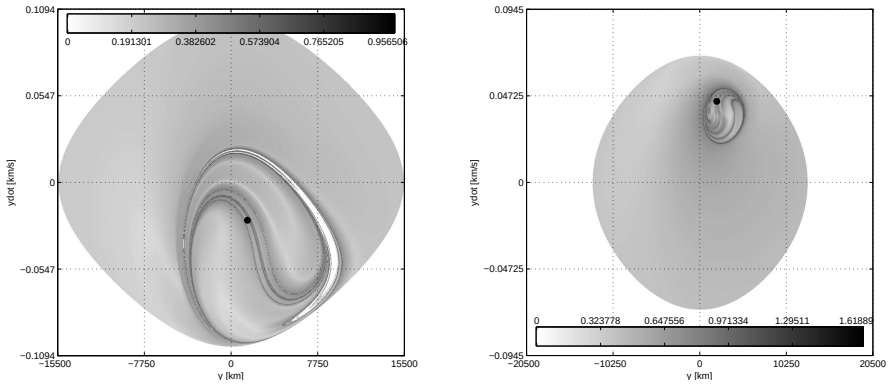

(a) Titania L_2 FTLE Gateway Map

(b) Oberon L_1 FTLE Gateway Map

(c) Flow Toward Oberon: Isosurface of FTLE Slices

(d) Alternate View of (c)

Figure 11. Maps of FTLE Values Constructed Near Titania and Oberon and x–y–$\dot{y}$ FTLE Tubes

area of particular numerical sensitivity is apparent in Figure 11(a) as a solid white curve of FTLE values interior to the main lobe. This white region, as well as the areas beyond the larger gray shape on both maps, reflect FTLE values set to zero based on integration issues or exclusion by the CRP zero–velocity bounds. Through inspection and observation of various trajectories, regions are revealed by the FTLE maps where trajectories enter the nearby Uranian moon's neighborhood, and do not subsequently exit (for the duration of the simulation). Carefully selecting from among these values, the trajectories marked on Figure 11 with large black dots are isolated. These trajectories appear in Figure 12 colored from green to red with increasing time.

*Given the significant computational cost to construct FTLE maps, the generation of multiple map slices in x is accelerated with a massively parallel computation implemented on a graphics processing unit (∼100× speedup over a comparable CPU implementation). From these slices that constitute an FTLE volume around the Uranus–Oberon L_1 point, the major features consistent with the outermost ridge in the interior of Figure 11(b) are recovered using an isosurface extraction.

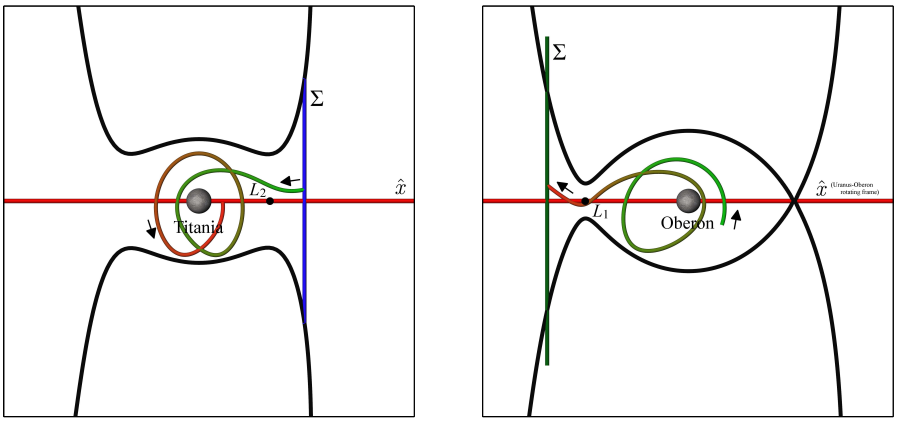

(a) Terminal Segment In Uranus–Titania Rotating Frame (b) Initial Segment in Uranus–Oberon Rotating Frame

Figure 12. Transfer "Bookends"—Originating Near Oberon and Terminating Near Titania

These initial segments and the corresponding FTLE maps are each calculated with the associated primary acting as P_2 in the four–body system. For example, the Oberon segment and map are calculated in the Uranus–Oberon rotating frame with Titania orbiting counter–clockwise "interior" to Oberon. In this case, Titania's motion initiates at an angle of $-\frac{\pi}{4}$ radians with respect to the Uranus–Oberon rotating x axis. Similarly, for the Titania segment, Oberon orbits the system "exterior" to Titania. However, Oberon orbits in a clockwise direction given a slower angular rate than Titania.

To simplify the analysis, the initial Oberon map state is transformed into the Uranus–Titania rotating frame using transformation matrices similar to those in Anderson[40] and, subsequently, evolved backward in time to verify its consistency under the alternate system. All additional analysis occurs in the Uranus–Titania rotating frame. Next, the states from the two map points are evolved forward in time from the vicinity of Oberon and backward in time from the vicinity of Titania. These propagations are terminated after successive intersections with the negative x–axis segment colored magenta in Figure 13. This selection of the intersection region is inspired by Koon et al.[33] The forward propagation from the vicinity of Oberon always begins with Oberon at $\frac{\pi}{4}$ rad in the Uranus–Titania rotating frame. The first crossings of the forward and backward propagations are displayed in Figure 13(a), and subsequent crossings in both forward and backward time are displayed, for illustration, in Figure 13(b). The backward propagation of the Oberon trajectory (from Figure 12(b)) in the Uranus–Titania–Oberon four–body system appears at the top of the figures initially colored black. Oberon's circular path is represented in gold, while the spacecraft trajectory segments are colored using a discrete rotating color scheme that increments with each full nondimensional time unit (or $\sim$1.38 days) as a means to aid in the time correlation. Forward and backward segments colored in different colors upon intersection immediately reveal a timing mismatch.

For the backward propagation from Titania to be valid, the initial angular position of Oberon must be adjusted. This adjustment is accomplished by summing the time required for the forward propagation from Oberon to the n^{th} crossing with the length of time required for the backward propagations to meet the x axis. Given the total "inner" time duration (the forward time from the Oberon section plus the backward time from the Titania section), the angular position of Oberon is adjusted using its constant angular rate. However, the adjusted initial position impacts the time for the backward propagations to reach the x axis, so this adjustment procedure must be iterated until the timing and the initial Oberon position agree. In some cases, close primary passages cause this iterative process to diverge. Consequently, only some combinations of forward and backward crossings are attainable. Finally, it must be verified that the Titania end–segment (and, indirectly, the FTLE map) remains valid for the adjusted Oberon positions. Fortunately, the proximity to Titania generally overwhelms the perturbation from Oberon—its effects are still visible but, for each of the

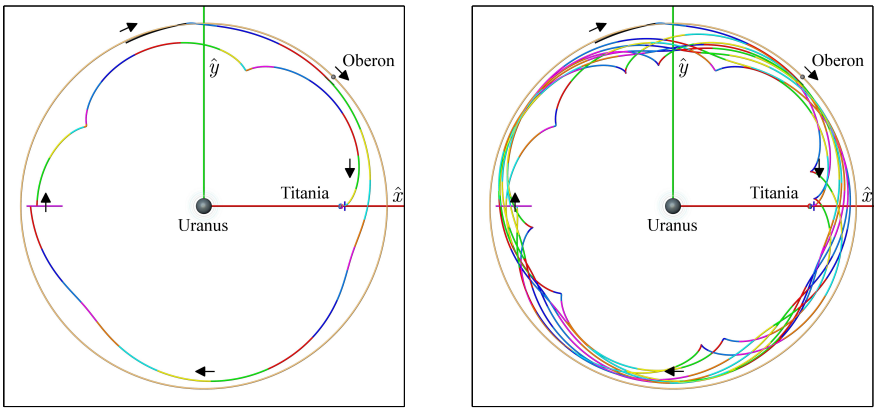

(a) The First Crossings

(b) Several Subsequent Crossings for Illustration

Figure 13. Negative x–axis Trajectory Crossings

sampled cases, the selected trajectory remains qualitatively consistent. Given corrected timing and angular positions for Oberon, the Cauchy–Green tensor and its eigenvalue/eigenvector sets can be computed. Due to the sensitivity associated with the timing and position of P_4, the present analysis is restricted to perturbations in velocity space along the associated eigenvector components. Moreover, the maximum perturbation associated with the segments is frequently 1×10^{-2} or about 36 $\frac{\text{m}}{\text{s}}$ to induce sufficient stretching, i.e., the end points of the segments represent a 36 $\frac{\text{m}}{\text{s}}$ change in velocity. In Figure 14, the forward crossing of the segment is colored red, and the matching backward crossings, when they exist, are colored in blue for the first crossing, and then in black for subsequent attainable crossings.

Inspection of the resulting intersections reveals multiple connections. However, the new "time–to–crossing" associated with the perturbed states that should ultimately lead to an intersection must be incorporated. Careful adjustment may preserve the trajectory connection, but significant deflection after exposure to the third primary gravity field may destroy the intersection. An iterative process or a scheme that directly employs the timing and initial position of P_4 may help. Recall that this particular system is selected primarily because of the significant effects of the third primary, so challenges are to be expected. Notwithstanding these difficulties, linked trajectories that preserve their continuity can still be identified. For example, in Figure 15, three forward crossings and a single backward crossing satisfy the timing requirement to maintain an end–to–end solution. This solution requires 7.6 $\frac{\text{m}}{\text{s}}$ to depart the vicinity of Oberon, 20.1 $\frac{\text{m}}{\text{s}}$ upon arrival at Titania, and 143.7 $\frac{\text{m}}{\text{s}}$ to adjust $\dot{y}$ at the intersection point for a total of 171.4 $\frac{\text{m}}{\text{s}}$. The time–of–flight is 382.77 days. This particular example serves to illustrate that the control segment concept can benefit from flow–based information. Additionally, it demonstrates that the methodology can be extended to more complex models. As the complexity increases, additional tools may alleviate or avoid some of the challenges inherent in nonautonomous flows.

Additional insight from orthogonality considerations of CG eigenvectors

In planar flows, LCS have been demonstrated to act as finite–time invariant manifolds. As a consequence, even in complex, time–dependent flows structures can be identified that bound and govern the motion. These structures offer useful channels for transport trajectories. Efforts are currently ongoing, with significant interest, to extend these concepts to higher–dimensional flows. Blazevski and Haller supply a rigorous treatment on the identification of transport barriers in three–dimensional flows.[1] Some of the ideas in that work and related extensions, indicate the potential usefulness for identifying flow governing structures by enforcing orthogonality conditions. This theory is still under development, but the associated concepts aid in a clearer understanding of flow behavior. A highly idealized example of these considerations is illustrated in Figure 16

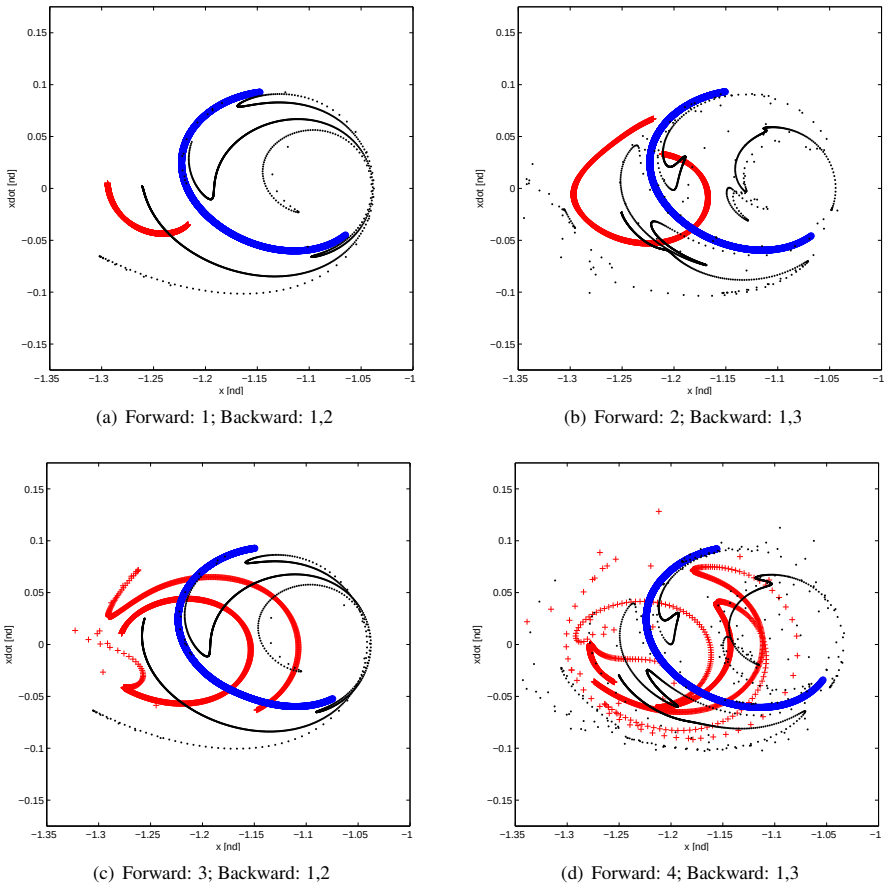

(a) Forward: 1; Backward: 1,2

(b) Forward: 2; Backward: 1,3

(c) Forward: 3; Backward: 1,2

(d) Forward: 4; Backward: 1,3

Figure 14. Crossing Combinations: The n^{th} forward crossings of the ξ_4 velocity aligned segments from the Oberon region are marked with red crosses, while the first backward crossings from the Titania region are marked with blue circles, and the subsequent computable backward crossings are marked with black points.

where a known Lagrangian coherent structure corresponding to the stable P_1 manifold branch of a L_1 Lyapunov orbit (i.e., a flow separatrix) in the four–dimensional, Earth–Moon planar CR3BP is depicted in blue. The eigenvectors tied to the largest eigenvalue of the CGST (both senses) are plotted in red. The (unrepresented) fourth dimension corresponds to a Poincaré map hyperplane defined as $x = 0$. Various operations yield a set of associated vectors that are plotted tangential to the LCS in cyan. Such a process, intimates the possibility of identifying similar structures in systems without knowledge of flow separating characteristics.

CONCLUSION

The ability to identify flow regions that are generally advantageous to mission goals in complex astrodynamical systems expedites the search for viable options in a wide range of design scenarios. In the case of maneuvers, knowledge of the flow behavior offers the opportunity to save propellant and time. The information supplied by the CGST augments and generalizes well–known methods that employ the state transition matrix for trajectory design and analysis. Since employing maneuvers in phase–space regions reflecting large stretching behavior produces larger effects downstream for smaller expense, FTLE ridges represent advantageous choices for maneuver placement. Specifically, control segments informed by the system flow supply

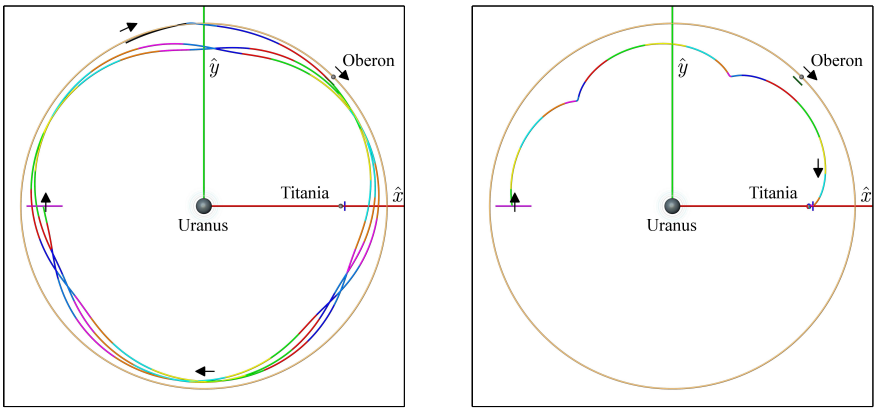

(a) Three Forward Crossings

(b) One Backward Crossing

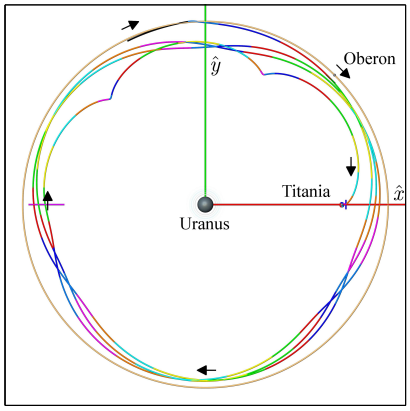

(c) Complete Transfer Trajectory

Figure 15. FCS Identified System–to–system Transfer

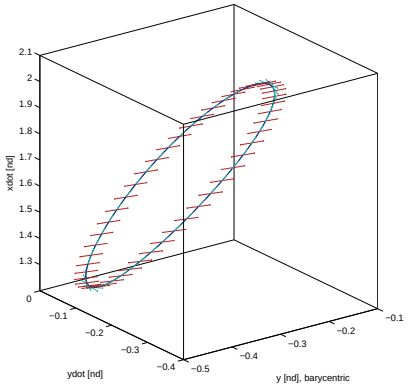

Figure 16. LCS and Associated Vectors in the Earth–Moon CR3BP

excellent candidates for optimal maneuver options. Lagrangian coherent structures, their underlying theory, and the related mathematical tools characterize the flow in a system and offer this valuable context.

ACKNOWLEDGMENTS

The authors wish to acknowledge Ms. Amanda Haapala and Ms. Natasha Bosanac for insight and assistance with the numerical correction of some of the trajectories as well as Mr. Rohan Sood for proofreading the document. This work is supported by the Rune and Barbara Eliasen Aerospace Visualization Laboratory at Purdue University. The facilities of the Eliasen lab have been leveraged heavily for computation and the production of visuals for this paper. Support for this effort from the Purdue University College of Engineering is also acknowledged and appreciated.

REFERENCES

[1] D. Blazevski and G. Haller, "Hyperbolic and Elliptic Transport Barriers in Three–Dimensional Unsteady Flows," *Physica D*, 2013. Submitted.

[2] G. Haller, "Distinguished material surfaces and coherent structures in three–dimensional fluid flows," *Physica D*, Vol. 149, 2001, pp. 248–277.

[3] H. Teramoto, G. Haller, and T. Komatsuzaki, "Detecting invariant manifolds as stationary Lagrangian coherent structures in autonomous dynamical systems," *Chaos*, Vol. 23, 2013, pp. 043107–1–12, http://dx.doi.org/10.1063/1.4824314.

[4] E. S. Gawlik, J. E. Marsden, P. C. du Toit, and S. Campagnola, "Lagrangian coherent structures in the planar elliptic restricted three–body problem," *Celestial Mechanics and Dynamical Astronomy*, Vol. 103, No. 3, 2009, pp. 227–249.

[5] C. R. Short, K. C. Howell, and X. M. Tricoche, "Lagrangian Coherent Structures in the Restricted Three–Body Problem," *AAS/AIAA Space Flight Mechanics Meeting*, New Orleans, Louisiana, February 2011.

[6] D. Pérez, G. Gómez, and J. J. Masdemont, "Detecting Invariant Manifolds Using Hyperbolic Lagrangian Coherent Structures," *1st IAA/AAS Conference on the Dynamics and Control of Space Systems*, Porto, Portugal, March, 2012.

[7] C. R. Short and K. C. Howell, "Lagrangian Coherent Structures in Various Map Representations for Application to Multi–Body Gravitational Regimes," *Acta Astronautica*, Vol. 94, No. 2, 2014, pp. 592–607, http://dx.doi.org/10.1016/j.actaastro.2013.08.020.

[8] T. Peacock and G. Haller, "Lagrangian coherent structures: The hidden skeleton of fluid flows," *Physics Today*, February 2013, pp. 41–47.

[9] G. Haller and F. J. Beron-Vera, "Geodesic theory of transport barriers in two–dimensional flows," *Physica D*, Vol. 241, 2012, pp. 1680–1702.

[10] C. G. Schroer and E. Ott, "Targeting in Hamiltonian systems that have mixed regular/chaotic phase spaces," *Chaos*, Vol. 7, No. 4, 1997, pp. 512–519.

[11] D. Grebow, *Trajectory Design in the Earth–Moon System and Lunar South Pole Coverage*. Ph.D. thesis, Purdue University, West Lafayette, Indiana, 2010.

[12] G. Haller, "Finding finite–time invariant manifolds in two–dimensional velocity fields," *Chaos*, Vol. 10, No. 1, 2000, pp. 99–108.

[13] G. Haller and G. Yuan, "Lagrangian coherent structures and mixing in two–dimensional turbulence," *Physica D*, Vol. 147, 2000, pp. 352–370.

[14] G. Haller, "Lagrangian coherent structures from approximate velocity data," *Physics of Fluids*, Vol. 14, No. 6, 2002, pp. 1851–1861.

[15] M. Mathur, G. Haller, T. Peacock, J. Ruppert-Felsot, and H. Swinney, "Uncovering the Lagrangian Skeleton of Turbulence," *Physical Review Letters*, Vol. 98, 2007, pp. 144502–1–4.

[16] G. Haller, "A variational theory of hyperbolic Lagrangian Coherent Structures," *Physica D*, Vol. 240, 2011, pp. 574–598.

[17] M. Farazmand and G. Haller, "Computing Lagrangian Coherent Structures from Variational LCS theory," *Chaos*, Vol. 22, No. 013128, 2012.

[18] C. Garth, F. Gerhardt, X. Tricoche, and H. Hagen, "Efficient Computation and Visualization of Coherent Structures in Fluid Flow Applications," *IEEE Transactions on Visualization and Computer Graphics*, Vol. 13(6), 2007, pp. 1464–1471.

[19] T. Peacock and J. Dabiri, "Introduction to focus issue: Lagrangian coherent structures," *Chaos*, Vol. 20, 2010, pp. 017501–1–3.

[20] R. L. Anderson, M. W. Lo, and G. H. Born, "Application of Local Lyapunov Exponents to Maneuver Design and Navigation in the Three–Body Problem," *AAS/AIAA Astrodynamics Specialist Conference*, Big Sky, Montana, August 2003.

[21] G. Harden, *Automated Patch Point Placement for Autonomous Spacecraft Trajectory Targeting* M.S. thesis, School of Aeronautics and Astronautics, Purdue University, West Lafayette, Indiana, 2013.

[22] G. K. Harden, A. F. Haapala, K. C. Howell, and B. G. Marchand, "Automated Patch Point Placement for Spacecraft Trajectory Targeting," *AAS/AIAA Space Flight Mechanics Meeting*, Santa Fe, New Mexico, January 2014.

[23] M. Lara, R. P. Russell, and B. Villac, "Classification of the Distant Stability Regions at Europa," *Journal of Guidance, Control, and Dynamics*, Vol. 30, No. 2, 2007, pp. 409–418.

[24] B. F. Villac, "Using FLI maps for preliminary spacecraft trajectory design in multi–body environments," *Celestial Mechanics and Dynamical Astronomy*, Vol. 102, No. 1–3, 2008, pp. 29–48.

[25] B. Villac and S. Broschart, "Applications of Chaoticitiy Indicators to Stability Analysis Around Small Bodies," *AAS/AIAA Space Flight Mechanics Meeting*, Savannah, Georgia, February, 2009.

[26] K. Oshima and T. Yanao, "Applications of Gravity Assists in the Bicircular and Bielliptic Restricted Four–body Problem," *AAS/AIAA Space Flight Mechanics Meeting*, Santa Fe, New Mexico, January 2014.

[27] D. R. Smith, *An Introduction to Continuum Mechanics — after Truesdell and Noll*. Dordrecht: Kluwer Academic Publishers, 1993.

[28] G. Haller and T. Sapsis, "Lagrangian Coherent Structures and the Smallest Finite–Time Lyapunov Exponent," *Chaos*, Vol. 21, No. 023115, 2011, pp. 1–7.

[29] T. Shinbrot, E. Ott, C. Grebogi, and J. A. Yorke, "Using chaos to direct trajectories to targets," *Physical Review Letters*, Vol. 65, 1990, pp. 3215–3218.

[30] D. Eberly, R. Gardner, B. Morse, and S. Pizer, "Ridges for Image Analysis," *Journal of Mathematical Imaging and Vision*, Vol. 4, 1994, pp. 355–371.

[31] F. Diacu, "The Solution of the *n*–body Problem," *The Mathematical Intelligencer*, Vol. 18, No. 3, 1996, pp. 66–70.

[32] V. Szebehely, *Theory of Orbits: The Restricted Problem of Three Bodies*. New York: Academic Press, 1967.

[33] W. S. Koon, M. W. Lo, J. E. Marsden, and S. D. Ross, "Constructing a Low Energy Transfer Between Jovian Moons," *Contemporary Mathematics*, Vol. 292, 2002, pp. 129–145.

[34] D. Blazevski and C. Ocampo, "Periodic orbits in the concentric circular restricted four–body problem and their invariant manifolds," *Physica D*, Vol. 241, 2012, pp. 1158–1167.

[35] J. Guzman, *Spacecraft Trajectory Design in the Context of a Coherent Restricted Four–Body Problem*. Ph.D. thesis, Purdue University, West Lafayette, Indiana, 2001.

[36] T. A. Pavlak and K. C. Howell, "Evolution of the Out–of–Plane Amplitude for Quasi–Periodic Trajectories in the Earth–Moon System," *Acta Astronautica*, Vol. 81, No. 2, 2012, pp. 456–465.

[37] D. C. Davis and K. C. Howell, "Characterization of Trajectories Near the Smaller Primary in the Restricted Problem for Applications," *Journal of Guidance, Control, and Dynamics*, Vol. 35(1), 2012, pp. 116–128.

[38] T. Pavlak, *Trajectory Design and Orbit Maintenance Strategies in Multi-Body Dynamical Regimes*. Ph.D. thesis, Purdue University, West Lafayette, Indiana, 2013.

[39] C. Geisel, *Spacecraft Orbit Design in the Circular Restricted Three–Body Problem Using Higher–Dimensional Poincaré Maps*. Ph.D. thesis, Purdue University, West Lafayette, Indiana, 2013.

[40] R. L. Anderson, *Low Thrust Trajectory Design for Resonant Flybys and Captures Using Invariant Manifolds*. Ph.D. thesis, University of Colorado, Boulder, Colorado, 2005.